



Mesoscale structure, mechanics, and transport properties of source rocks' organic pore networks

Jeremie Berthonneau^{a,1,2}, Amaël Obliger^{a,1}, Pierre-Louis Valdenaire^a, Olivier Grauby^b, Daniel Ferry^b, Damien Chaudanson^b, Pierre Levitz^c, Jae Jin Kim^d, Franz-Josef Ulm^e, and Roland J.-M. Pellenq^{a,b,e}

^aMultiScale Material Science for Energy and Environment (<MSE>²), Massachusetts Institute of Technology, Cambridge, MA 02139; ^bCNRS, UMR 7325, Aix-Marseille Université, Centre Interdisciplinaire de Nanoscience de Marseille (CINaM), 13288 Marseille Cedex 9, France; ^cCNRS, UMR 8234, Université Pierre et Marie Curie, Physicochimie des Electrolytes et Nanosystèmes Interfaciaux (PHENIX), 75252 Paris Cedex 5, France; ^dShell Technology Center at Houston, Shell International Exploration and Production Inc., Houston, TX 77082; and ^eDepartment of Civil and Environmental Engineering, Massachusetts Institute of Technology, Cambridge, MA 02139

Edited by Michael L. Klein, Temple University, Philadelphia, PA, and approved October 18, 2018 (received for review May 15, 2018)

Organic matter is responsible for the generation of hydrocarbons during the thermal maturation of source rock formation. This geochemical process engenders a network of organic hosted pores that governs the flow of hydrocarbons from the organic matter to fractures created during the stimulation of production wells. Therefore, it can be reasonably assumed that predictions of potentially recoverable confined hydrocarbons depend on the geometry of this pore network. Here, we analyze mesoscale structures of three organic porous networks at different thermal maturities. We use electron tomography with subnanometric resolution to characterize their morphology and topology. Our 3D reconstructions confirm the formation of nanopores and reveal increasingly tortuous and connected pore networks in the process of thermal maturation. We then turn the binarized reconstructions into lattice models including information from atomistic simulations to derive mechanical and confined fluid transport properties. Specifically, we highlight the influence of adsorbed fluids on the elastic response. The resulting elastic energy concentrations are localized at the vicinity of macropores at low maturity whereas these concentrations present more homogeneous distributions at higher thermal maturities, due to pores' topology. The lattice models finally allow us to capture the effect of sorption on diffusion mechanisms with a sole input of network geometry. Eventually, we corroborate the dominant impact of diffusion occurring within the connected nanopores, which constitute the limiting factor of confined hydrocarbon transport in source rocks.

porous media | electron tomography | mechanics | fluid transport | mesoscale

The emergence of disruptive technology (1, 2) in the field of petroleum engineering has improved access to hydrocarbons from source rock formations. As a result, the historically declining production of natural gas has been on the rise. The stimulation technique of hydraulic fracturing aims to create a fracture network accessing the hydrocarbons and to force their migration to the crack's surface (2, 3). However, as the bimodal production curves suggest, the large-scale deployment of hydraulic fracturing wells has led to invariably declining heterogeneous production rates (4–6). Early stages of these rates follow a square root of time drop, which in the long term becomes an exponential decay leading to limited production. The production of hydraulic fracturing wells depends on three factors: the capacity of creating fracture networks successfully reaching the confined hydrocarbons, the ability of maintaining these fractures opened, and the fluid transport properties of the materials storing hydrocarbons (4–7). At the molecular scale, hydrocarbons are generated within organic agglomerates—typically referred to as kerogens—composed of an amorphous porous carbon skeleton and dispersed in a fine-grained mineral matrix (7). The chemical composition of the carbon skeleton (carbon hybridization, functional groups) is known to evolve through thermal maturation induced during geological burial (8, 9). It is therefore imperative to establish a

deep scientific understanding of the structural, mechanical, and confined fluid transport properties of these organic agglomerates with respect to their thermal maturation. This type of knowledge would allow predictions of the displacement of confined hydrocarbons from the organic matter to fracture networks and their contribution in the production of hydraulic fracturing wells.

Realistic atomistic-scale models of kerogens have begun being utilized to simulate hybridization of the carbon skeletons upon maturation (8). These chemical transitions strengthen the kerogen matrix and shift the rupture mechanism from a plastic to the brittle state. In addition, the structural arrangement of nanopores is responsible for their strong adsorption, the breakdown of continuum hydrodynamics, and the occurrence of interfacial wetting effects in agreement with the fast productivity declines of exploitation wells (10, 11). Such nanostructures demonstrate a self-diffusion governed transport regime (12). These recent breakthroughs, however, only account for the subnanopores network reached through atomistic-scale models (8). The presence of hierarchical structures of organic hosted pores evolving through thermal maturation, as probed in scanning electron microscopy (5, 13), small-angle neutron scattering (14–17), and adsorption (3, 14, 18), may affect the overall properties. For example, at an experimental macroscopic scale, the organic porosity has been found to be responsible for a significant reduction of the kerogen particle modulus with respect to thermal

Significance

In source rocks, natural hydrocarbons are generated from organic matter dispersed in a fine-grained mineral matrix. The potential recovery of hydrocarbons is therefore influenced by the geometry of the organic hosted porous networks. Here, the three-dimensional structures of such networks are revealed using electron tomography with a subnanometer resolution. The reconstructions are first characterized in terms of morphology and topology and then used to build a multiscale simulation tool to study the mechanics and the transport properties of confined fluids. Our results offer evidence of the prevalent role of connected nanopores, which subsequently constitutes a material limit for long-term hydrocarbon production.

Author contributions: J.B., A.O., P.-L.V., O.G., F.-J.U., and R.J.-M.P. designed research; J.B., A.O., and P.-L.V. performed research; D.C., P.L., and J.J.K. contributed new reagents/analytic tools; J.B., A.O., P.-L.V., O.G., and D.F. analyzed data; and J.B., A.O., P.-L.V., and R.J.-M.P. wrote the paper.

The authors declare no conflict of interest.

This article is a PNAS Direct Submission.

This open access article is distributed under [Creative Commons Attribution-NonCommercial-NoDerivatives License 4.0 \(CC BY-NC-ND\)](https://creativecommons.org/licenses/by-nc-nd/4.0/).

¹J.B. and A.O. contributed equally to this work.

²To whom correspondence should be addressed. Email: berthonneau@cinam.univ-mrs.fr.

This article contains supporting information online at www.pnas.org/lookup/suppl/doi:10.1073/pnas.1808402115/-DCSupplemental.

Published online November 15, 2018.

maturation (19). In addition, the analysis of gas adsorption isotherms demonstrates that thermal maturity of the organic matter affects the surface area, pore volume, and geometrical permeability (3, 14, 18, 20). However, any interpretation of adsorption data is restricted by the simplistic assumptions adopted in the models. The issue thus becomes the validity of results from both theoretical and experimental studies, which cannot be reliable without an accurate determination of geometrical arrangements of the organic pore networks at relevant scales (21).

Recent developments of bright-field electron tomography allow imaging pores of amorphous materials with sizes above 0.5 nm in three dimensions (21, 22). Such resolution overlaps with atomistic-scale models and permits a consistent multiscale approach. In this paper, we provide 3D reconstructions of the organic pore network of one oil-prone and two gas-prone source rocks with subnanometer resolution. We show that the parameters extracted from the analysis of the tomograms compare reasonably well to those measured with N₂ adsorption isotherms. This approach therefore offers an insight on the evolution of the organic pore networks in terms of structural, mechanical, and fluid transport properties at different thermal maturities. We demonstrate that the structural evolution affects not only an average pore radius and geometric surface area, but more importantly the tortuosity and connectivity. Through imaging informed simulation procedure, we further reveal that these topological features impact both mechanical and transport properties. We show that the mesoscale a maturation-induced decrease of rigidity. This offset the strengthening of carbon matrix as noted through reactive potential atomistic-scale models (8). In addition, following the previous work in this field (23–25), we study the influence of pressurized fluid inside pore networks, which leads to different stress distributions that impact crack nucleation areas. Combined with the recent findings on hydrocarbon transport within atomistic simulations of nanostructures (10–12), our analysis allows us to capture the effect of sorption on diffusion mechanisms with just a single input of the porous network geometry. As a conclusion, we show how the diffusion, occurring in the connected nanopores, constitutes the limiting factor of confined hydrocarbon transport, despite the consideration of sorption. The multiscale simulation approach presented here hence provides a way to access the interplay between topology and physical properties of porous solids at the mesoscale.

Results

We first performed adsorption isotherms on three samples from economically valuable source rock formations containing type II kerogens: Marcellus (MAR), Haynesville (HAY), and Lower Eagle Ford (LEF). The organic geochemistry of these samples (*SI Appendix, Table S1*) plotted in the modified Van Krevelen diagram (26) illustrates their differences in terms of hydrocarbon generation potentials (*SI Appendix, Fig. S1B*). In brief, LEF is a source rock entering the oil window whereas HAY and MAR are source rocks in the dry gas window. The specific surface areas (A_s), pore volumes (V_p), and hydraulic radii (r_H) obtained from N₂ adsorption analyses are summarized in *SI Appendix, Table S2*. The specific surface area increases with thermal maturity, which leads to decrease in the average pore size ($r_H = 4V_p/A_s$) (*SI Appendix, Fig. S1C*). This aligns with previous studies performed on extended sets of shale gas plays (3, 14, 17). These results suggest that (i) the geothermal maturation (transition from oil-prone to gas-prone) triggers the formation of organic hosted nanopores (3, 13) and (ii) our source rocks samples correspond to the two extremes of this general tendency.

To further test this hypothesis, we performed direct observations and analysis of the pore networks. Among the organic agglomerates dispersed in source rocks, the migrated organic matter (solid bitumen and/or pyrobitumen) is recognized as the main contributor of organic hosted porosity (13). Focused ion beam (FIB) thin sections were extracted on those locations in each sample and their tridimensional structures were reconstructed through electron

tomography (*SI Appendix*). Fig. 1 *A–C* shows the tridimensional pore aperture maps of the electron tomograms of LEF, HAY, and MAR, respectively. Significantly different structures are readily observable, as evidenced by the decreasing ranges of aperture radii. The resulting pore-size distributions (PSDs), plotted in Fig. 1*D*, confirm this qualitative description. LEF presents a convex PSD with pore radii in the range of 3–12.6 nm, while HAY and MAR expose concave distributions dominated by nanopores ($0.5 < r < 2.0$ nm). It is worth noting that our field of view precludes the observation of pore with $r > 20$ nm, which impacts the PSD. Nonetheless, these distributions agree with previous findings that present decrease of the average pore size (*SI Appendix, Fig. S1C*) with respect to thermal maturity (3, 13, 14).

The in-pore chord length distribution (CLD) is recognized as an effective stereological tool for characterizing disordered porous media (27–29). The endpoints of frequency distribution segments appear at the pore interface, $f_p(r)$, and therefore were computed within the tomograms (Fig. 1*E*). LEF showed a constant distribution below 1 nm, which decreases slightly in the range of 1–11 nm, followed by a sharp decay. In HAY and MAR, the distributions are constant at $r < 1.5$ nm and exhibit abrupt decays at larger values of r . The specific surface area, A_s , can be extracted from the first moment of the in-pore CLD using the following equation (28):

$$A_s = \frac{4\varphi_{meso}}{\rho_s(1 - \varphi_{meso}) \langle \ell \rangle}, \quad [1]$$

where φ_{meso} is the porosity of the tomogram, ρ_s is the density of the solid phase, and $\langle \ell \rangle$ is the first moment of the normalized CLD. The porosity (φ_{meso}) was measured by the ratio of pore volume with the total volume of the tomogram. The density of the amorphous carbon matrix (ρ_s) was arbitrarily estimated as $\rho_s = 1.0$ g/cm³ for LEF and $\rho_s = 1.4$ g/cm³ for HAY and MAR (8). If A_s is plotted as a function of the shortest chord length r_c (Fig. 1*F*), then the geometrical surface area (S^{geo}) can be defined by extrapolating r_c to zero (29) using Eq. 2:

$$A_s = \frac{S^{geo}}{\alpha r_c + 1}, \quad [2]$$

where the constant α equals 1.15, 0.55, and 0.95 nm⁻¹ for LEF, HAY, and MAR, respectively. From this expression, we obtain $S^{geo} = 113$ m²/g for LEF, 217 m²/g for HAY, and 338 m²/g for MAR, which is in a reasonable agreement with values measured in gas adsorption experiments (*SI Appendix, Table S2*). Small discrepancies between specific surface areas obtained from adsorption isotherms and geometrically determined values were previously documented for mesoporous materials and evaluated at ~20% (30), with S^{geo} being greater than A_s . Despite the differences between two approaches, the results confirm the increase of accessible surface area as a function of thermal maturity and the predominance of subnanopores in MAR and HAY with respect to LEF. This decrease in average pore size can be reasonably related to the development of subnanopores within the organic agglomerate as it is converted to mobile alkanes such as methane (3).

One advantage of the 3D porous network reconstructions is the ability to directly measure their topological properties. The tortuosities calculated from random walkers traveling through pore networks were 1.9 ± 0.7 , 3.7 ± 0.5 , and 6.6 ± 0.7 for LEF, HAY, and MAR, respectively (*SI Appendix, Fig. S3*). These mean values increase with thermal maturity, whereas their SDs are related to the variance in PSD (31). Other studies have previously demonstrated that the geometrical permeability, k , ($k = \varphi r_H^2/\xi$) of organic porous networks increases with maturity (3) [where ξ is the Kozeny dimensionless constant determined

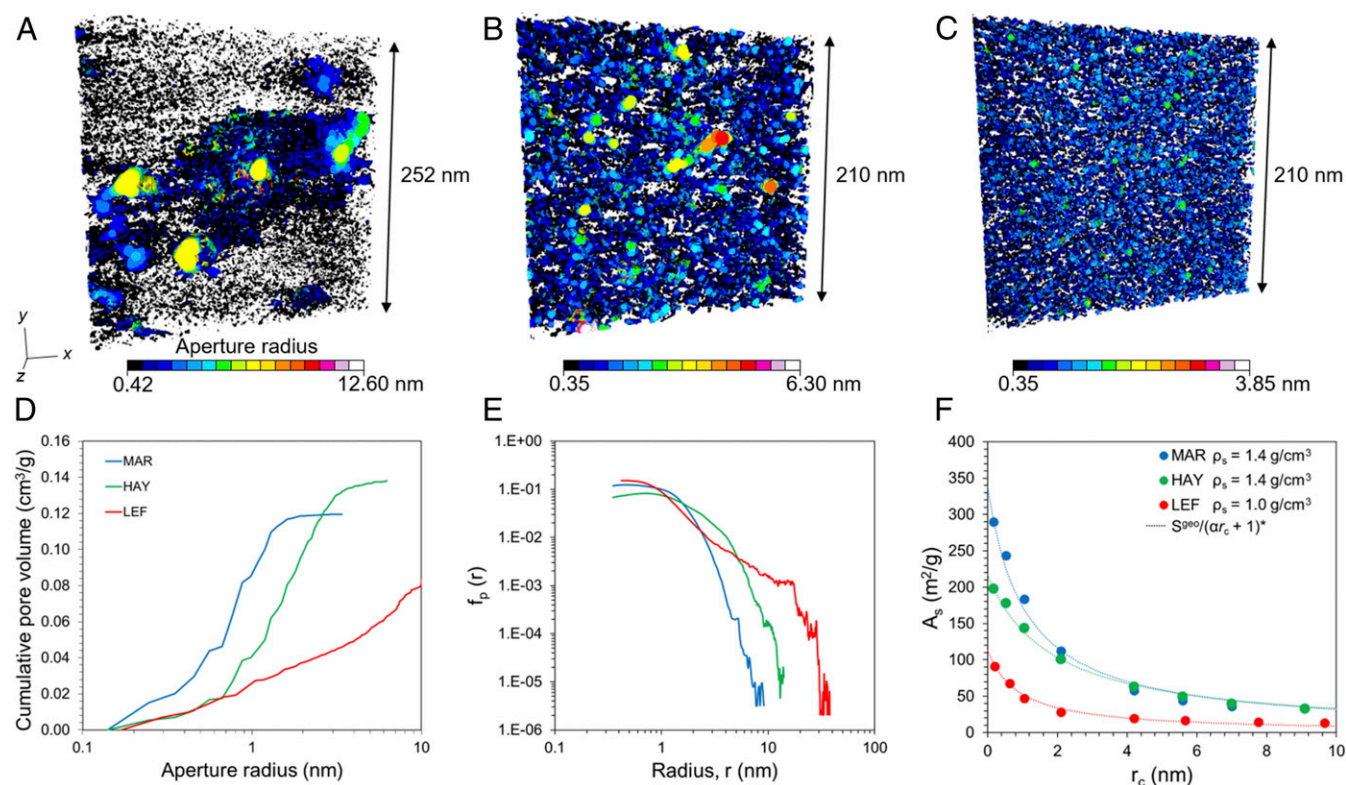


Fig. 1. Morphological characterization of the organic mesoporous networks imaged in electron tomography. Aperture maps of the organic pore networks of (A) LEF ($\phi_{\text{meso}} = 9.1\%$), (B) HAY ($\phi_{\text{meso}} = 19.3\%$), and (C) MAR ($\phi_{\text{meso}} = 16.9\%$). (D) Pore-size distributions from aperture maps calculation. (E) In-pore CLDs. (F) Specific surface areas (A_s) calculation from Eq. 1 as a function of the cutoff distance (r_c) of the in-pore C.L.D.

from flow core plug experiments (32)]. The evolution of permeability was interpreted as the result of a significant decrease in tortuosity (reduction of ξ by a factor of 4–8). Contradictory to previous findings, we show that the tortuosity measured on the organic porous network of three source rocks increases with thermal maturity (*SI Appendix, Fig. S3*). In parallel, the connectivity density (ζ), obtained with the ratio of the first Betti number and the total volume of the tomogram (33), increase with maturity (*SI Appendix, Fig. S3*). This trend also rationalizes the differences observed between S^{geo} and A_s at low maturity (LEF), where a significant part of the pore network is disconnected and thus inaccessible to N_2 molecules. This indicates that the thermal evolution of the organic matter not only entails morphological changes of the porous network (decreasing of r_H and concomitant increasing of S^{geo}) as shown previously (3, 14), but it also implies major topological changes toward increasingly connected networks. We emphasize that these topological features impact the porosity detected in transmission electron microscopy, including organic nanopores ($r < 1$ nm) that mainly connect the organic mesopores ($r > 1$ nm).

The next step is to utilize a numerical approach to study the mechanical behavior and the confined hydrocarbons transport at the mesoscale. Lattice models were created by converting voxels of the binarized tomograms to lattice nodes corresponding to void, if porosity is detected, and the organic carbon skeleton (8). The mechanical, transport, and thermodynamical properties of the organic carbon skeleton presented hereafter take into account results from molecular dynamics using realistic numerical models of kerogen (8).

We used a fast Fourier transform (FFT)-based numerical method (34–36) to compute the elastic response of the lattice models from LEF and MAR (*SI Appendix, Eq. S3*). We arbitrarily assigned to the organic carbon skeleton a local Young's

modulus of 2 GPa for LEF and 15 GPa for MAR with a Poisson's ratio of 0.25 for both, in agreement with published data from molecular simulations on oil-prone (37) and gas-prone kerogens (8). Assuming the same Poisson's ratio at the box scale, the global Young's moduli resulting from the simulations are 1.4 GPa and 6.9 GPa for LEF and MAR, respectively. Considering the linear elasticity, the ratio between macro- and micro-Young's moduli (i.e., the decrease of rigidity) constitutes the main relevant quantity. It comes to 70% for LEF and down to 46% for MAR. Since the porosity alone cannot explain this difference, we argue that the mesopore's topology is responsible for such decreases. The presence of a homogeneous and highly disordered porous network (Fig. 1C) therefore explains the counterintuitive link between the rigid organic carbon skeleton (8) of the gas-prone sample (MAR) and its flexible behavior at the upper scale. On the contrary, the oil-prone sample (LEF) presents a lower decrease in rigidity at the macroscopic scale due to heterogeneous distribution of pores, including isolated mesopores (Fig. 1A). This decrease of rigidity with thermal maturity is confirmed by experimental indentations (19).

In Fig. 2, we illustrate how the elastic energy is stored inside two mesostructures under agent (a), corresponding to an imposed averaged strain $\langle \epsilon_{ii} \rangle = 0.01$, and agent (b), including an adsorbed fluid characterized by a fluid pressure P . The total elastic energy, reduced per volume unit (10^6 J/m³), is 0.82 for LEF-(a), 0.9 for LEF-(b), 4.13 for MAR-(a), and 4.5 for MAR-(b). For (a) and (b) we observe a similar total stored energy for a given averaged strain. However, agent (a) leads to Gaussian energy distributions, whereas agent (b) leads to exponential energy distributions (Fig. 2). These two types of distributions have already been established in porous networks where it was shown that exponential distributions govern the crack initiation zones (38). This demonstrates that the pressurized fluid, not studied by classical tensile tests, is critical in predicting the mechanical

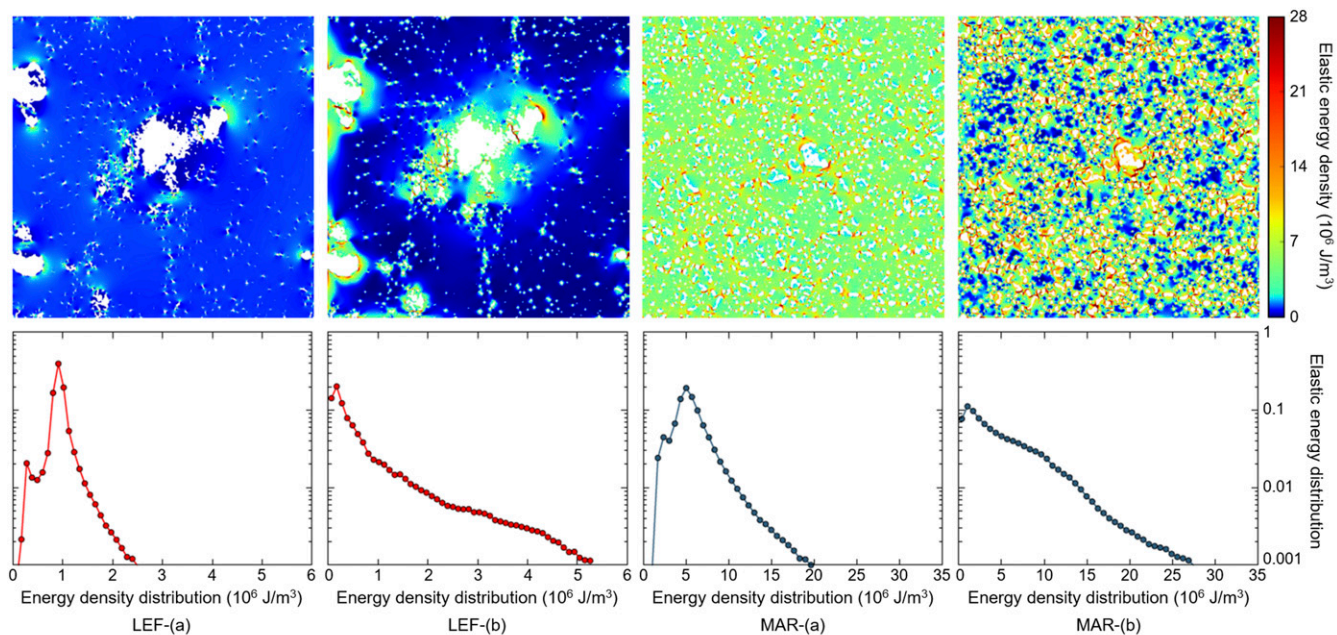


Fig. 2. Elastic simulations of the two porous mesostructures originating from LEF and MAR under two types of agent: (a) imposed strain boundary, and (b) adsorbed fluid with free strain boundary. The averaged strain of the simulation box is $\langle \epsilon_{ij} \rangle = 0.01$ for all cases. The size is 700×700 pixels with a resolution of 0.42 nm for LEF and 0.35 nm for MAR. Mesopore phase is in white. (Top) Elastic energy density fields (10^6 J/m^3). (Bottom) Distribution of the elastic energy density (10^6 J/m^3) for each simulation.

damage of organic matter contained in source rocks. In fact, hydraulic fracture propagation is directly influenced by stress distribution as crack nucleation appears more likely in high elastic energy areas. It corresponds to the vicinity of the largest pores for LEF-(b), leaving the rest of the matter undamaged. Contrary, crack nucleation can be more homogeneous at higher thermal maturity [see Fig. 2, MAR-(b)].

We applied the continuous time random walk (CTRW) (39–42) algorithm to study the confined hydrocarbons transport properties over the geometry given by the mesoscale lattice models. The

numerical scheme used here to simulate transport consists of constructing random walks, where walkers can move isotropically on the lattice. Because two different diffusion timescales are considered, one for each phase (i.e., the nanoporous and the mesoporous phases), we also assign random transit times at each step of the random walk from exponential distributions characterized by an average transit time that depends on the phase where the walker is located. To account for sorption between nano- and mesoporous phases, we use partial boundary conditions at the interface (see *SI Appendix* for more details on the homogenization

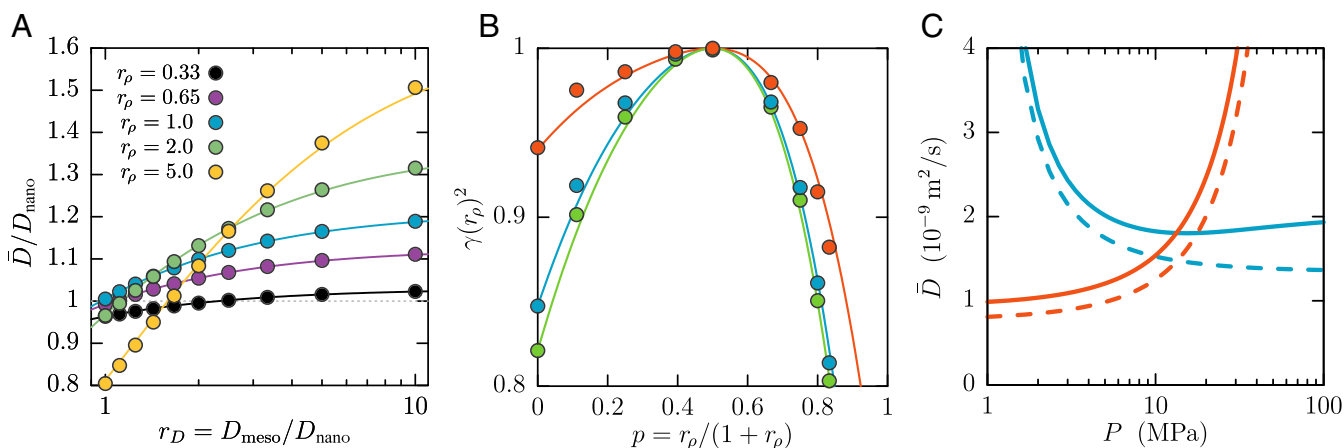


Fig. 3. Homogenized fluid transport properties of the mesoscale lattice models. (A) Homogenized diffusion coefficient of the MAR reconstruction scaled by D_{nano} as function of the diffusion contrast $r_D = D_{\text{meso}}/D_{\text{nano}}$ for different concentration ratios $r_\rho = \rho_{\text{meso}}/\rho_{\text{nano}}$ indicated by colors. The corresponding curves stand for the effective medium theory (Eq. 2) where the value of $\gamma(r_\rho)^2$ is \bar{D}/D_{nano} when $D_{\text{meso}} = D_{\text{nano}}$ (i.e., $r_D = 1$). (B) Concentration-dependent obstruction factor $\gamma(r_\rho)^2$ as function of the probability $p(r_\rho)$ for a random walker to cross the interface from the nano- to the mesoporous phase (red: LEF, green: HAY, blue: MAR). The corresponding curves display the analytical model (Eq. 4) where γ_0^2 is simply taken as $\gamma_0^2 = \gamma(p=0)^2$. (C) Homogenized diffusion coefficient of methane for LEF (red) and MAR (blue) as function of the bulk fluid pressure. The dashed curves correspond to the diffusion in the nanoporous phase only, while the solid lines represent the homogenized model with mesoporosity. Standard geological conditions ($T = 400 \text{ K}$ and lithostatic pressure of 25 MPa) have been considered.

procedure). Due to limited size of the mesopores and their connectivity through the nanoporous phase, where transport has been shown to be purely diffusive (10, 12, 42), we neglect advection in the system. Moreover, the amorphous nature of the nanoporous phase would prevent hydrodynamic slip at the interface. As a result, we treat both phases as homogeneous, which means that we attribute a single fluid concentration ρ_i and diffusion coefficient D_i per phase. Fig. 3A shows the homogenized diffusion coefficient, \bar{D} , adimensionned by D_{nano} as function of the diffusion ratio $r_D = D_{meso}/D_{nano}$ in the MAR case for various concentration ratios r_ρ . We observe that the upscaled diffusion coefficient increases with the diffusion ratio. We use an effective medium theory (EMT) (43, 44) to rationalize the dependence on r_D as

$$\frac{\bar{D}}{D_{nano}} = \frac{1 + r_\rho r_D}{1 + r_\rho r_D^{-1}} \gamma(r_\rho)^2, \quad [3]$$

where $r_\rho = \varphi/(1 - \varphi)$ is the ratio of the volume fractions of the mesoporous phase (φ) and the nanoporous phase ($1 - \varphi$), and $\gamma(r_\rho)^2$ is an obstruction factor that captures the impact of geometry and sorption at the interface on the homogenized diffusion coefficient. Fig. 3A reports an excellent agreement between numerical results and the EMT where $\gamma(r_\rho)^2$ is taken as $\bar{D}(r_D = 1)/D_{nano}$ for each curve. We notice that the influence of sorption depends nonmonotonically on the concentration ratio that controls the sorption effect.

Fig. 3B displays, for LEF, HAY, and MAR, an evolution of the obstruction factor (γ^2) as a function of, $p = r_\rho/(1 + r_\rho)$, the probability of a random walker crossing an interface from nano- to mesoporous phase. When $P = 0$ (or $\rho_{meso} = 0$) there is no fluid in the mesopores; $\gamma(p=0)^2 = \gamma_0^2$ is a constant that corresponds to the obstruction factor of the nanoporous phase, while the mesopores are considered as an impermeable phase. In practice, this can be computed by a simple random-walk simulation with bounce-back rules at the interface. If the concentration in mesopores increases and the probability p stays below 0.5, the diffusion increases due to an increased probability of the fluid entering mesopores. In this regime the fluid can use the mesopores as shortcuts, thus lowering the influence of the tortuosity of the nanoporous phase on the overall diffusion. When p gets closer to 0.5, the efficiency of the shortcut effect reaches a maximum because the decreasing probability of exiting from a mesopore balances the advantage of entering it. At $p = 0.5$, there is no influence of the interface because the probability of crossing the interface in both directions is the same, thus resulting in $\gamma = 1$. Beyond this point ($p > 0.5$), mesopores start to act as traps because the probability of entering a mesopore becomes larger than the probability of escaping it. The homogenized diffusion coefficient thus diminishes and ultimately goes to zero in the limit of perfect trapping ($p = 1$ or $r_\rho \rightarrow \infty$). An analytical model (SI Appendix) for the concentration-dependent obstruction factor becomes

$$\gamma(p)^2 = \frac{\gamma_0^2 + 4(1 - \gamma_0^2)p(1 - p) + p^3 \sqrt{4(1 - \gamma_0^2)} 4p(1 - p)}{1 + p^3 \sqrt{4(1 - \gamma_0^2)}}. \quad [4]$$

Fig. 3B shows an excellent agreement between the proposed model and numerical results. For three very different geometries, the model (Eq. 4) captures the effect of sorption on diffusion through p with only one parameter γ_0^2 , which depends on the geometry of the system.

We then compare, in Fig. 3C, the diffusion coefficient in a single nanoporous phase with the one accounting for the distribution of mesopores given by the tomograms as a function of pressure P of bulk methane in mesopores. For the diffusion coefficient in the nanoporous phase, we use a free volume theory. The methane concentration in the nanoporosity is given by a Langmuir

adsorption isotherm. Transport and adsorption behaviors in subnanopores for MAR were obtained by molecular simulation studies using the atomistic-scale model of Marcellus (8, 45). As a first approximation, we treat methane in mesopores as a bulk fluid. Bulk properties of methane, diffusion coefficient, and concentration as a function of P are taken from the National Institute of Standards and Technology database. For the MAR case, diffusion at low pressure is dominated by the nanoporous phase because of the strong heat of adsorption of nanopores due to confinement effects. Then, instead of decreasing exponentially with pressure, the diffusion model that accounts for mesopores reaches a minimum around 15 MPa and increases at higher pressure to become almost constant when P approaches 100 MPa (Fig. 3C). Consequently, the recovery of confined hydrocarbons is impacted at the mesoscopic level by nonmonotonic evolution of transport properties in time. We also report the same quantities in the LEF case but with diffusion in the nanoporous phase described by a more general free-volume model that accounts for adsorption-induced swelling (SI Appendix), which leads to an exponential increase as a function of pressure (46, 47). Due to swelling, the adsorption isotherm evolves linearly with P (until $P > 50$ MPa) (48), thus lowering the impact of sorption on transport at the mesoscale. As a result, mesopores do not induce a qualitative change on the transport behavior at the mesoscale. Quantitatively, in both cases, the application of the CRTW algorithm showed that the transport of confined hydrocarbons at the mesoscale is mainly dictated by the nanoporosity. If mesopores in the gas-prone (rigid) case can induce nonmonotonical trend for the diffusion coefficient, they do not induce that effect for the oil-prone case (flexible nanoporosity). At the engineering scale, these trends complement the effect of fractures on wells' productivity. As already pointed out in previous studies (49–51), the pressure dependence of fractures' permeability can lead to a decrease of productivity when pressure decreases. The diffusion mechanisms evidenced here would either accentuate the productivity decrease for oil-prone organic matter, or partially mitigate it for gas-prone organic matter.

Discussion

Bright-field electron tomography was applied on source rocks' organic matter, which allowed 3D reconstructions of the organic porous networks with a subnanometer resolution. Structural analysis of the tomograms demonstrated that thermal maturation entails increase of the accessible surface area, tortuosity, and connectivity of the nanoporous networks. Lattice models were then produced using the coupling between (i) geometrical arrangements of the porous networks at the mesoscale with (ii) nanoscale features deduced from a molecular dynamics study (8). These models allowed studying numerically an elastic response and the confined hydrocarbons transport properties at the mesoscale. Our results highlight the effect of topological changes on the organic matter rigidity. Moreover, we showed that pressurized fluid inside pore networks implies different potential crack nucleation areas, localized around the largest pores for the oil-prone case (LEF), and more homogeneously distributed at higher thermal maturity (MAR). The dominant impact of diffusion mechanisms occurring within the nanoporosity on confined hydrocarbon transport, previously sensed through atomistic studies, was also confirmed at the mesoscale. The constraint from imaging allowed a relatively simple computation of the only two parameters required by the fluid transport model: the volume fraction of the mesoporosity and the obstruction factor γ_0^2 of the nanoporous phase. These results have also led to some questions, specifically whether the evidenced mesoscale effects may be generalized to a larger ensemble of source rocks, and whether one can identify the key geochemical parameters of the thermal history triggering the

evolution. To conclude, the herein constructed analytical model can be readily used for predictions of “in-place” confined hydrocarbon recovery in multiscale approaches accounting for macropores, organic/inorganic interfaces, and fracture networks (52–54). This further improves the link between nanoscale constitutive models of porous materials (8, 10–12) and their engineering applications (4–6).

Materials and Methods

This study was conducted on samples from economically valuable source rock formations (MAR, HAY, and LEF). The thermal maturity was evaluated by RockEval pyrolysis and standard organic petrology technique. Low-pressure N₂ isotherms were performed at 77 K using a Micromeritics 3Flex. Thin sections of organic inclusions were extracted in an FEI Helios NanoLab 660 FIB. Electron tomography acquisitions were carried out with a transmission electron microscope (JEOL JEM 2011) fitted with a LaB₆ electron gun, under a 200-kV accelerating voltage, and assisted by the Digital Micrograph software (GATAN). The structural characterization was performed using iMorph

(imorph.sourceforge.net) and imageJ. Lattice models were then created by converting voxels of the tomograms to lattice nodes. An FFT-based numerical model was used to compute the elastic response under two different agents: (i) an imposed averaged strain, and (ii) an adsorbed fluid inside pores. The CTRW algorithm was finally used to study the transport properties over the geometry of the lattice models (see *SI Appendix* for complementary details on *Materials and Methods*).

ACKNOWLEDGMENTS. We thank Jacob Michael Sobstyl [Massachusetts Institute of Technology (MIT)-Civil and Environmental Engineering] for his help regarding the manuscript. This work has been carried out within the framework of the ICoME2 Labex (ANR-11-LABX-0053) and the A*MIDEX/Aix-Marseille University projects (ANR-11-IDEX-0001-02) cofounded by the French program “Investissements d’Avenir” managed by the ANR, the French National Research Agency. We acknowledge funding from Royal Dutch Shell and Schlumberger through the MIT X-Shale Hub as well as from Total through the MIT/CNRS FASTER-Shale project. We also thank Micromeritics Instrument Corp. for the generous gift of the 3Flex adsorption equipment.

- Kerr RA (2010) Energy. Natural gas from shale bursts onto the scene. *Science* 328:1624–1626.
- Cueto-Felgueroso L, Juanes R (2013) Forecasting long-term gas production from shale. *Proc Natl Acad Sci USA* 110:19660–19661.
- Valenza JJ, Drenzek N, Marques F, Pagels M, Mastarlerz M (2013) Geochemical controls on shale microstructure. *Geology* 41:611–614.
- Monteiro PJM, Rycroft CH, Barenblatt GI (2012) A mathematical model of fluid and gas flow in nanoporous media. *Proc Natl Acad Sci USA* 109:20309–20313.
- Silin D, Kneafsey T (2012) Shale gas: Nanometer-scale observations and well modelling. *J Can Pet Technol* 51:464–475.
- Patzek TW, Male F, Marder M (2013) Gas production in the Barnett shale obeys a simple scaling theory. *Proc Natl Acad Sci USA* 110:19731–19736.
- Vandenbroucke M, Largeau C (2007) Kerogen origin, evolution and structure. *Org Geochem* 38:719–833.
- Bousige C, et al. (2016) Realistic molecular model of kerogen’s nanostructure. *Nat Mater* 15:576–582.
- Tissot B, Welte D (1984) *Petroleum Formation and Occurrence* (Springer, Berlin).
- Falk K, Coasne B, Pellenq R, Ulm F-J, Bocquet L (2015) Subcontinuum mass transport of condensed hydrocarbons in nanoporous media. *Nat Commun* 6:6949.
- Lee T, Bocquet L, Coasne B (2016) Activated desorption at heterogeneous interfaces and long-time kinetics of hydrocarbon recovery from nanoporous media. *Nat Commun* 7:11890.
- Obliger A, Pellenq R, Ulm F-J, Coasne B (2016) Free volume theory of hydrocarbon mixture transport in nanoporous materials. *J Phys Chem Lett* 7:3712–3717.
- Louks RG, Reed RM, Ruppel SC, Jarvie DM (2009) Morphology, genesis, and distribution of nanometer-scale pores in siliceous mudstones of the Mississippian Barnett shale. *J Sediment Res* 79:848–861.
- Clarkson CR, et al. (2013) Pore structure characterization of North American shale gas reservoirs using USANS/SANS, gas adsorption, and mercury intrusion. *Fuel* 103:606–616.
- Mastarlerz M, He L, Melnichenko YB, Rupp JA (2012) Porosity of coal and shale: Insights from gas adsorption and SANS/USANS techniques. *Energy Fuels* 26:5109–5120.
- Thomas JJ, Valenza JJ, Craddock PR, Bake KD, Pomerantz AE (2013) The neutron scattering length density of kerogen and coal as determined by CH₃OH/CD₃OH exchange. *Fuel* 117:801–808.
- Gu X, et al. (2016) Quantification of organic porosity and water accessibility in Marcellus shale using neutron scattering. *Energy Fuels* 30:4438–4449.
- Wang Y, Zhu Y, Chen S, Li W (2014) Characteristics of the nanoscale pore structure in Northwestern human shale gas reservoirs using field emission scanning electron microscopy, high-pressure mercury intrusion, and gas adsorption. *Energy Fuels* 28:945–955.
- Zargari S, Wilkinson TM, Packard CE, Prasad M (2016) Effect of thermal maturity on elastic properties of kerogen. *Geophysics* 81:M1–M6.
- Happel J, Brenner H (1983) *Low Reynolds Number Hydrodynamics* (Martinus Nijhoff, Boston).
- Stoekel D, et al. (2014) Morphological analysis of disordered macroporous-mesoporous solids based on physical reconstruction by nanoscale tomography. *Langmuir* 30:9022–9027.
- Biermans E, Molina L, Batenburg KJ, Bals S, Van Tendeloo G (2010) Measuring porosity at the nanoscale by quantitative electron tomography. *Nano Lett* 10:5014–5019.
- Perkins TK, Kern LR, Aime M (1961) Widths of hydraulic fractures. *J Pet Technol* 13:937–949.
- Heider Y, Markert B (2017) A phase-field modeling approach of hydraulic fracture in saturated porous media. *Mech Res Commun* 80:38–46.
- Peng S, et al. (2018) Hydraulic fracture simulation with hydro-mechanical coupled discretized virtual internal bond. *J Petrol Sci Eng* 169:504–517.
- Van Krevelen DW (1961) *Coal: Typology, Chemistry, Physics, Constitution* (Elsevier, Amsterdam).
- Mering J, Tchoubar D (1968) Interprétation de la diffusion centrale des rayons X par les systèmes poreux. *J Appl Cryst* 1:153–165.
- Pellenq RJ-M, Levitz P (2002) Capillary condensation in a disordered mesoporous medium: A grand conical Monte Carlo study. *Mol Phys* 100:2059–2077.
- Ioannidou K, et al. (2016) Mesoscale texture of cement hydrates. *Proc Natl Acad Sci USA* 113:2029–2034.
- Coasne B, Galarneau A, Di Renzo F, Pellenq RJ-M (2010) Molecular simulation of nitrogen adsorption in nanoporous silica. *Langmuir* 26:10872–10881.
- Gostovic D, Smith JR, Kundinger DP, Jones KS, Wachsmann ED (2007) Three-dimensional reconstruction of porous LSCF cathodes. *Electrochem Solid State Lett* 10:B214–B217.
- Ozgunus T, Mobedi M, Ozkol U (2014) Determination of Kozeny constant based on porosity and pore to throat size ratio in porous medium with rectangular rods. *Eng Appl Comput Fluid Mech* 8:308–318.
- Odgaard A, Gundersen HJG (1993) Quantification of connectivity in cancellous bone, with special emphasis on 3-D reconstructions. *Bone* 14:173–182.
- Moulinec H, Suquet P (1995) A FFT-based numerical model for computing the mechanical properties of composites from images of their microstructures. *IUTAM Symposium on Microstructure-Property Interactions in Composites Materials* (Springer, Dordrecht, The Netherlands), pp 235–246.
- Moulinec H, Suquet P (1998) A numerical method for computing the overall response of nonlinear composites with complex microstructures. *Comput Methods Appl Mech Eng* 157:69–94.
- Schneider M, Ospald F, Kabel M (2016) Computational homogenization of elasticity on a staggered grid. *Int J Numer Methods Eng* 105:693–720.
- Collell J, et al. (2014) Molecular simulation of bulk organic matter in type II shales in the middle of the oil formation window. *Energy Fuels* 28:7457–7466.
- Laubie H, Radjai F, Pellenq R, Ulm F-J (2017) Stress transmission and failure in disordered porous media. *Phys Rev Lett* 119:075501.
- Montroll EW, Weiss GH (1965) Random walks on lattices. II. *J Math Phys* 6:167–181.
- Kenkre VM, Montroll EW, Shlesinger MF (1973) Generalized master equations for continuous-time random walks. *J Stat Phys* 9:45–50.
- Dentz M, Guze P, Russian A, Dweik J, Delay F (2012) Diffusion and trapping in heterogeneous media: An inhomogeneous continuous time random walk approach. *Adv Water Resour* 49:13–22.
- Lee SB, Kim IC, Miller CA, Torquato S (1989) Random-walk simulation of diffusion-controlled processes among static traps. *Phys Rev B Condens Matter* 39:11833–11839.
- Kalnin JR, Kotomin E (1998) Modified Maxwell-Garnett equation for the effective transport coefficients in inhomogeneous media. *J Phys Math Gen* 31:7227–7234.
- Kalnin JR, Kotomin EA, Maier J (2002) Calculations of the effective diffusion coefficient for inhomogeneous media. *J Phys Chem Solids* 63:449–456.
- Obliger A, Ulm F-J, Pellenq R (2018) Impact of nanoporosity on hydrocarbon transport in shales’ organic matter. *Nano Lett* 18:832–837.
- Fujita H (1993) Free volume interpretation of the polymer effect on solvent dynamics. *Macromolecules* 26:643–646.
- Hsu J-P, Lin S-H (2005) Diffusivity of solvent in a polymer solution-expansive free volume effect. *Eur Polym J* 41:1036–1042.
- Obliger A, et al. (October 23, 2018) Poroelectricity of methane-loaded mature and immature kerogen from molecular simulations. *Langmuir*, 10.1021/acs.langmuir.8b02534.
- Walsh JB (1981) Effect of pore pressure and confining pressure on fracture permeability. *Int J Rock Mech Min Sci Geomech Abstr* 18:429–435.
- Wang C, Wu YS, Xiong Y, Winterfeldt PH, Huang Z (2015) Geomechanics coupling simulation of fracture closure and its influence on gas production in shale gas reservoirs. *SPE Reservoir Simulation Symposium*. Available at <https://www.onepetro.org/conference-paper/SPE-173222-MS>. Accessed August 23, 2018.
- Wheaton R (2017) Dependence of shale permeability on pressure. *SPE Reservoir Eval Eng* 20:228–232.
- Striolo A, Cole DR (2017) Understanding shale gas: Recent progress and remaining challenges. *Energy Fuels* 31:10300–10310.
- Apostolopoulou M, Stamatakis M, Striolo A (2017) A kinetic Monte Carlo framework for multi-phase fluid transport in heterogeneous pore networks. *J Chem Phys* 147:134703.
- Backeberg NR, et al. (2017) Quantifying the anisotropy and tortuosity of permeable pathways in clay-rich mudstones using models based on X-ray tomography. *Sci Rep* 7:14838.